



CeO₂ nanocrystal-modified layered MoS₂/g-C₃N₄ as 0D/2D ternary composite for visible-light photocatalytic hydrogen evolution: Interfacial consecutive multi-step electron transfer and enhanced H₂O reactant adsorption



Chengzhang Zhu^a, Yuting Wang^a, Zhifeng Jiang^b, Fanchao Xu^a, Qiming Xian^{a,*}, Cheng Sun^a, Qing Tong^c, Weixin Zou^{c,*}, Xiaoguang Duan^d, Shaobin Wang^d

^a State Key Laboratory of Pollution Control and Resource Reuse, School of the Environment, Nanjing University, Nanjing, 210023, PR China

^b Institute for Energy Research, Jiangsu University, Zhenjiang, 212013, PR China

^c Jiangsu Key Laboratory of Vehicle Emissions Control, Center of Modern Analysis, Nanjing University, Nanjing, 210093, PR China

^d School of Chemical Engineering and Advanced Materials, The University of Adelaide, Adelaide, SA, 5005, Australia

ARTICLE INFO

Keywords:

CeO₂ nanocrystals
2D layered MoS₂/g-C₃N₄
Multi-step electron transfer
Water splitting
H₂O reactant adsorption

ABSTRACT

Developing low-cost and high-performance catalysts is significant to solar-to-fuel conversion. Here, the synthesis of zero-dimensional (0D) CeO₂ nanocrystal-decorated two-dimensional (2D) layered hybrids of MoS₂/g-C₃N₄ was reported for the first time. In the absence of noble-metal cocatalyst, the optimized ternary CeO₂@MoS₂/g-C₃N₄ still manifested high photocatalytic activity toward H₂ generation, with a rate of 65.4 μmol/h, which is approximately 8.3 and 17.5-fold greater than g-C₃N₄ and CeO₂, respectively. The corresponding apparent external quantum efficiency reached 10.35% at a wavelength of 420 nm. The superior photocatalytic behavior of CeO₂@MoS₂/g-C₃N₄ heterojunction could be ascribed to the positive synergistic effects of well-matched energy-level positions and effective charge separation arose from the multi-step electron transfer processes between Ce⁴⁺/Ce³⁺ reversibility pairs and heterostructures. Furthermore, the adsorption ability of reactant H₂O molecules on CeO₂@MoS₂/g-C₃N₄ was investigated. Due to the interfacial electronic interaction and Ce³⁺ species, CeO₂@MoS₂/g-C₃N₄ presented more reaction active sites with enhanced adsorption capacity and decreased energy barrier for reactant H₂O molecules adsorption, which collaboratively promoted photocatalytic water splitting. This study provides new insights into the rational design of inexpensive ternary photocatalyst with multilevel electron transfer for efficiently converting solar energy into hydrogen without noble metals.

1. Introduction

In the wake of global energy and environmental crisis, supplying clean flue and energy on a practical scale and in a sustainable manner has become one of the frontier research fields [1–3]. Inspired by natural photosynthesis, solar-driven water splitting to produce hydrogen (H₂) using semiconductor photocatalysts is an effective and promising technique to realize the long-term solar-to-fuel conversion [4,5]. Ceria (CeO₂), a rare earth element of the lanthanide series, shows wide industrial applications, especially for vehicle exhaust purification and photocatalytic H₂ evolution, owing to its unique 4f electron structure, strong redox ability, and oxygen storage capacity [6–8]. However, the intrinsic properties of narrow solar spectral response and high recombination rate of the photoinduced carriers severely limits the H₂

production activity of CeO₂ [9,10]. To this end, enormous efforts have been dedicated to finding solutions to tackle the above-mentioned issues. Coupling CeO₂ with semiconductors with suitable bandgaps to construct heterostructures is conducive to broaden visible light absorption of CeO₂-based composites and efficiently accelerate interfacial charge separation, thus enhancing the photocatalytic efficiency.

Two-dimensional (2D) layered nanomaterials possess various fascinating properties, such as short carrier diffusion distance, large surface area, and superior electronic conductivity [11–14]. In particular, the recent investigations of graphic carbon nitride (g-C₃N₄) has attracted tremendous interest as a novel 2D metal-free organic polymer with the merits of unique s-triazine structure, proper band edges, high chemical stability, and easy production from nitrogen-rich precursors [15–19]. Moreover, g-C₃N₄ nanosheets (NSs) can provide a well-

* Corresponding authors.

E-mail addresses: xianqm@nju.edu.cn (Q. Xian), wxzou2016@nju.edu.cn (W. Zou).

defined support for fabrication of heterojunctions with abundant coupling heterointerfaces, enabling abundant surface-reactive sites [20]. Intensive studies focused on the formation of heterojunctions including $\text{TiO}_2/\text{g-C}_3\text{N}_4$ [21], $\text{CaIn}_2\text{S}_4/\text{g-C}_3\text{N}_4$ [22], and $\text{Bi}_2\text{MoO}_6/\text{g-C}_3\text{N}_4$ [23], with the purpose of overcoming the inherent demerits of $\text{g-C}_3\text{N}_4$. These binary systems exhibit enhanced visible-light photocatalytic performance towards water splitting compared to the single components. This is ascribed to the intimate interfacial contacts and well-matched band structures, which facilitated the separation of photogenerated charge carriers and subsequent photocatalytic reactions. Despite those attractive superiorities, low-cost and high-performance $\text{g-C}_3\text{N}_4$ -based composites for H_2 evolution should be further explored toward practical applications and commercial benefits.

As an alternative to noble metals cocatalysts (such as Pt, Rh, Pd), molybdenum disulfide (MoS_2) with a sandwich-like structure of three stacked atomic layers (S-Mo-S) linked by the van der Waals forces, has been proved to be an efficiency cocatalyst for H_2 generation because the existence of unsaturated Mo and S atoms at the exposed edges are capable of promoting the activity of edging sulfurs [24–27]. Furthermore, the introduction of black MoS_2 significantly increases the visible light absorption and reduces the reflection of light, hereby providing more free carriers for photocatalytic water splitting. More importantly, the analogous layered structures of MoS_2 and $\text{g-C}_3\text{N}_4$ can not only minimize the lattice mismatch, but also form a newly built-in electronic field at the interface of 2D-2D heterojunctions, favoring the separation efficiency of charges and surface reaction [28,29]. Therefore, it is anticipated that substantially enhanced H_2 evolution photoactivity of the elaborately desired $\text{CeO}_2@\text{MoS}_2/\text{g-C}_3\text{N}_4$ heterojunctions with rich $\text{Ce}^{3+}/\text{Ce}^{4+}$ reversibility pairs and intimate interfacial interactions can be achieved.

Herein, we present a gentle way to construct zero-dimensional (0D) CeO_2 nanocrystals (NCs) onto the surface of 2D layer-structured $\text{MoS}_2/\text{g-C}_3\text{N}_4$ nanosheets. To the best of our knowledge, no prior work of constructing such ternary composites has been reported for H_2 production from photocatalytic water splitting. Regarding the band alignment of the aforementioned three components, a consecutive multistep electron-transfer process was induced to endow a faster electron-hole separation in $\text{CeO}_2@\text{MoS}_2/\text{g-C}_3\text{N}_4$, instead of conventional single-step transfer. Reliance on the ternary heterostructure, stronger interfacial effects, relatively shorter charge-diffusion distance, more Ce^{3+} /oxygen vacancies, and abundant intimate contact interfaces would be simultaneously obtained, which primarily contributed to the superior photocatalytic activity and photostability under visible light irradiation. In addition, the charge transfer process was studied by the steady-state photoluminescence and transient photocurrent analysis, and the mechanism of water splitting over $\text{CeO}_2@\text{MoS}_2/\text{g-C}_3\text{N}_4$ heterojunction was also proposed.

2. Experimental section

2.1. Materials

Cerium nitrate hexahydrate ($\text{Ce}(\text{NO}_3)_3 \cdot 6\text{H}_2\text{O}$), sodium hydroxide (NaOH), sodium molybdate dihydrate ($\text{Na}_2\text{MoO}_4 \cdot 2\text{H}_2\text{O}$), dimethyl sulfoxide (DMSO), absolute ethanol ($\text{C}_2\text{H}_5\text{OH}$), toluene, butylamine, urea, and L-cysteine were purchased from Sinopharm Chemical Reagent Co., Ltd. All chemicals used are of analytical grade. Ultrapure water ($18.2\text{ M}\Omega\text{ cm}$) was supplied by a Simplicity UV ultrapure water system (Merck Millipore).

2.2. Synthesis of CeO_2 NCs

$\text{Ce}(\text{NO}_3)_3 \cdot 6\text{H}_2\text{O}$ (1 mmol) was ultrasonically dispersed in toluene solution, and then 0.15 mL butylamine was slowly dropped under vigorous agitation. Then, the above mixture was transferred into a 50 mL Teflon-lined autoclave and maintained at 180°C for 24 h. After being

cooled naturally, the resultant precipitate was repeatedly washed with ultrapure water until $\text{pH} = 7$ before being fully dried at 60°C . Then, the final samples were calcined in static air at 450°C for 3 h.

2.3. Loading CeO_2 NCs onto layer-structured $\text{MoS}_2/\text{g-C}_3\text{N}_4$ NSs

Graphite-like $\text{g-C}_3\text{N}_4$ was obtained by directly heating urea at 600°C for 4 h in a tube furnace. The ternary composite of $\text{CeO}_2@\text{MoS}_2/\text{g-C}_3\text{N}_4$ was synthesized using a feasible ultrasonic chemical method. Typically, 0.05 g $\text{g-C}_3\text{N}_4$ powder was dispersed into 30 mL DMSO under ultrasonication for 1 h. Subsequently, $\text{Na}_2\text{MoO}_4 \cdot 2\text{H}_2\text{O}$ (0.5 mmol) was dissolved in the L-cysteine solution, which was added dropwise into the faint yellow suspension, followed by hydrothermal treatment. After repeated washing and oven drying, an appropriate amount of layered $\text{MoS}_2/\text{g-C}_3\text{N}_4$ and fresh CeO_2 NCs (0.01 g) were dispersed in 50 mL methanol in an ultrasonic bath for 1 h, then vigorously stirred overnight in a fume hood to remove the solvent. Finally, the products were grounded and further calcined under N_2 flow at 300°C for 1 h to strengthen the interactions between the $\text{MoS}_2/\text{g-C}_3\text{N}_4$ nanostructure and CeO_2 matrix.

2.4. Characterization

The morphologies and particle sizes of the synthesized catalysts were examined on a transmission electron microscopy (TEM, JEM-200CX) at an acceleration voltage of 200 kV. X-ray diffraction (XRD) was characterized by a Philips X'Pert Pro diffractometer equipped with Ni-filtered $\text{Cu-K}\alpha$ radiation ($\lambda = 1.5418\text{ nm}$). X-ray photoelectron spectroscopy (XPS, ESCA PHI500) was used to examine the surface chemical composition and valence band (VB). Brunauer–Emmett–Teller (BET) surface areas were measured by nitrogen adsorption at 77 K on a Micromeritics ASAP 2010 adsorption apparatus. The optical properties of samples in the range of 200–800 nm were analyzed by a UV-vis spectrophotometer diffuse reflectance spectroscopy (DRS, UV-3600Plus) with BaSO_4 as the reference. Photoluminescence (PL) spectra were detected on a HORIBA Fluorolog 3-22-type fluorescence spectrophotometer with an excitation wavelength of 325 nm. Fourier transform infrared spectroscopy (FTIR) was employed as KBr discs on a Nicolet NEXUS470 FTIR (Thermo Scientific, USA) spectrometer. Electron paramagnetic resonance (EPR) spectra were recorded on JEOL JESFA200 EPR spectrometers. Water contact angles were measured by an optical tensiometer (OneAttension, Kruss scientific instrument) using the sessile drop method.

The electrochemical measurements were performed on a Shanghai Chenhua CHI660D instrument with a standard three-electrode cell. The as-prepared photocatalysts were spin-coated onto the indium tin oxide (ITO, $1 \times 2\text{ cm}^2$) as the working electrodes, while the saturated Ag/AgCl and Pt wire served as the reference electrode and counter electrode, respectively. The modified electrodes were prepared as follows: 5 mg of the catalyst was dispersed in 2 mL of ethanol to produce a slurry, which was then spread onto the ITO slice. Next, the above working electrodes were dried in an oven at 80°C for 1 h. A 500 W Xe arc lamp was utilized as the light source for irradiation throughout the electrochemical experiments.

2.5. Photocatalytic water splitting for H_2 evolution

The photocatalytic water-splitting reaction was carried out in a 100 mL Pyrex flask connected to a gas-closed circulation and evacuation system. As the light source, UV light emitting diodes (UV-LEDs) (3 W, Shenzhen LAMPLIC Science Co. Ltd. China) with an irradiation intensity at 80.0 mW cm^{-2} , equipped with the 420 nm cutoff filter were positioned 1 cm away from the reactor in four vertical directions. In a typical procedure, 50 mg of sample was dispersed and vigorously stirred in 80 mL of aqueous solution containing 0.5 M Na_2SO_3 and 0.5 M Na_2S . Prior to irradiation, the suspension was sonicated for 10 min,

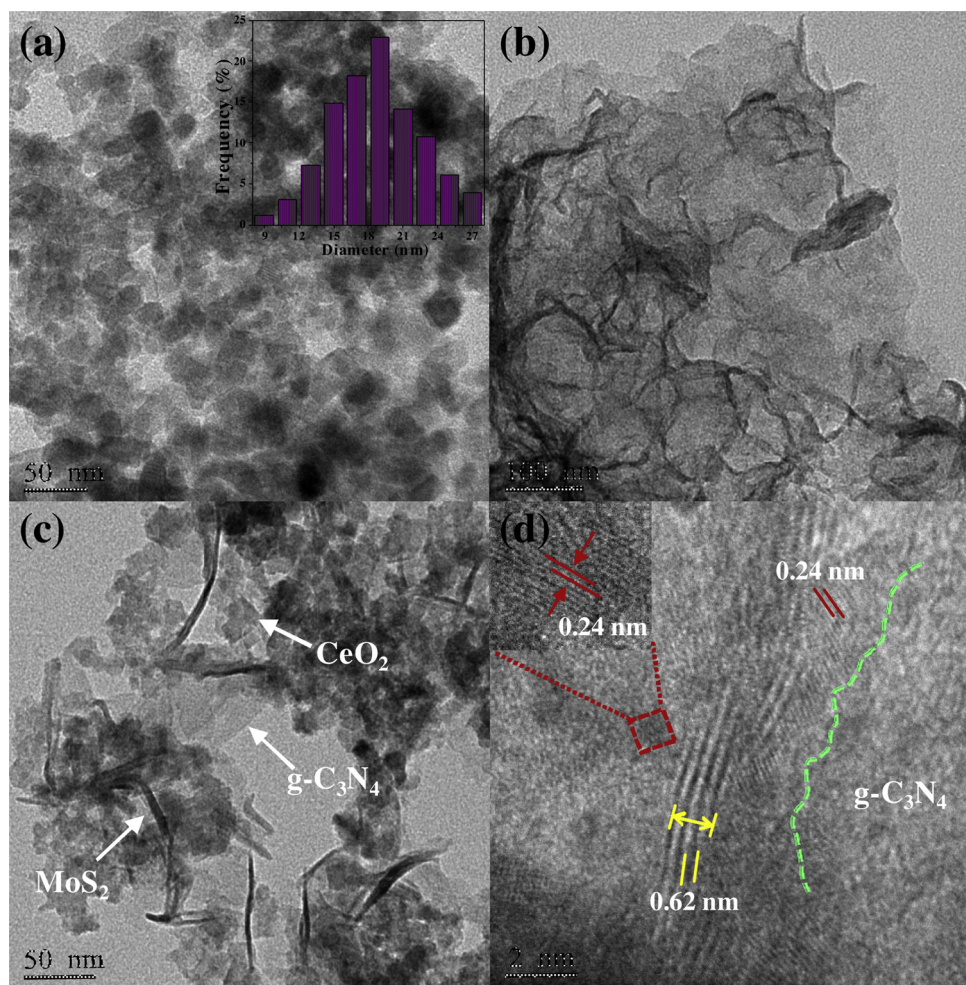


Fig. 1. TEM images of (a) CeO₂ NCs (inset: particle size distribution), (b) MoS₂/g-C₃N₄ NSs, and (c) CeO₂@MoS₂/g-C₃N₄. HRTEM image (d) of the CeO₂@MoS₂/g-C₃N₄ heterojunction.

subsequently purged with nitrogen for 30 min to completely remove the dissolved oxygen, ensuring an anaerobic condition and uniform irradiation of homogeneous suspension during the hydrogen evolution reaction. A 0.4 mL gas was intermittently sampled once an hour, and the amount of H₂ evolved was analyzed on-line by gas chromatography (GC-14C, Shimadzu, Japan, TCD, with nitrogen as the carrier gas and 5 Å molecular sieve column). The external quantum efficiency (QE) was measured and calculated from the equation of QE = 2 × number of evolved H₂ molecules/number of incident photons.

3. Results and discussion

3.1. Morphological, structural, and compositional information

The morphology and nanostructure of pristine CeO₂, MoS₂/g-C₃N₄, and CeO₂@MoS₂/g-C₃N₄ composite were investigated by TEM. As illustrated in Fig. 1a, CeO₂ is entirely consisted of numerous nanocrystals with an average diameter of around 19.7 nm. Apparent 2D layered structure of MoS₂ and g-C₃N₄ can be observed in Fig. 1b, and the well-defined two components are tightly cross-linked to each other, which might be beneficial for the rapid charge transfer across the interface [17,30]. Previous studies have reported that g-C₃N₄ is an ideal platform for loading nanosized catalysts because of the functional amino groups and large accessible surface, which favor the construction of heterojunction architecture [31–33]. As expected, Figs. 1c and S1 exhibit the TEM images of the resulting ternary CeO₂@MoS₂/g-C₃N₄ at different magnifications, in which the layered MoS₂/g-C₃N₄ serves as ideal

support for CeO₂ NCs to form an intimate heterojunction. Additionally, the elemental mapping of CeO₂@MoS₂/g-C₃N₄ (Fig. S2) displays the homogenous distribution of Mo, S, C, N, O, and Ce, confirming the fine interfacial contacts between three moieties. Moreover, the lattice spacings of 0.24 and 0.62 nm in the HRTEM image (Fig. 1d) correspond to the (200) and (002) planes of CeO₂ and MoS₂, respectively, while the blurry region below the indigo dash line is g-C₃N₄ because of its poor crystallinity [34,35]. Therefore, a close neighborhood of CeO₂, MoS₂, and g-C₃N₄ is achieved by an epitaxial growth process, which may favor the interfacial consecutive electron transfer to improve the charge migration and photocatalytic efficiencies.

To obtain the crystalline structure of different samples, XRD test was conducted (Fig. 2a). Typically, the diffraction peaks of CeO₂ NCs can be indexed to the cubic phase with the lattice constants of $a = b = c = 5.41 \text{ \AA}$ (space group $Fm\bar{3}m$, JCPDS card no. 34-0394) [36,37]. As for bare MoS₂, all the peaks accord with the typical patterns of the hexagonal 2H MoS₂ structure (JCPDS card no. 37-1492) [38]. g-C₃N₄ exhibits two distinct peaks at 13.1° and 27.4°, corresponded to the (100) and (002) crystal planes with in-plane structure packing units and the interlayer stacking interactions [39]. Notably, the XRD patterns of the composites are similar to that of CeO₂, and no characteristic peaks belonging to MoS₂ and g-C₃N₄ can be found despite their appearance in the TEM images (Fig. 1c and d). This is probably owing to the relatively low diffraction intensity and loading amount of MoS₂ and g-C₃N₄. To confirm the presence of both MoS₂ and g-C₃N₄ in the obtained CeO₂@MoS₂/g-C₃N₄ composite, XPS analysis was further performed. Obvious peaks in the survey spectra (Fig. 2b) demonstrate the existence of Ce, O,

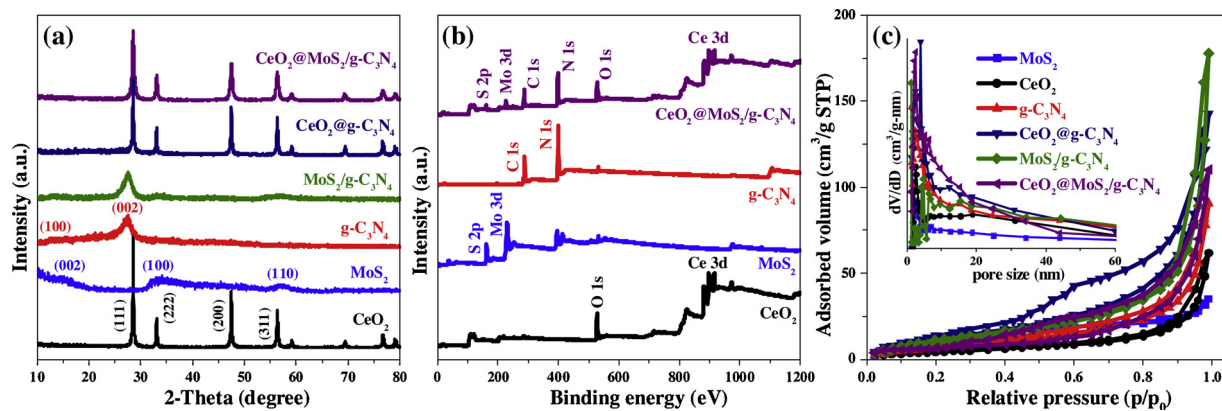


Fig. 2. (a) XRD patterns, (b) XPS surveys, (c) N₂ adsorption-desorption isotherms and pore size distribution plot (inset) of different samples.

C, N with a small amount of Mo and S elements, suggesting that both g-C₃N₄ and MoS₂ were successfully hybridized with CeO₂.

It is generally accepted that the high specific surface area (SSA), superior light-harvesting capacity and rapid charge separation are of vital importance to the photocatalytic activity [20,40]. The textural and structural properties of the obtained samples were studied using N₂ sorption isotherms (Fig. 2c), and the corresponding SSA, pore volume, and pore size distribution are summarized in Table S1. It is found that the ternary composite of CeO₂@MoS₂/g-C₃N₄ possesses a decreased SSA (83 m² g⁻¹) compared to 2D layered MoS₂/g-C₃N₄ (93 m² g⁻¹), which might be ascribed to the decoration of CeO₂ NCs which increases the weight of MoS₂/g-C₃N₄ NSs. However, the H₂ production efficiency of CeO₂@MoS₂/g-C₃N₄ (as shown in the following) reaches a maximum, indicating that in the work, the SSA is not the decisive factor to determine the photocatalytic efficiency. Based on the TEM and XPS analysis, it is reasonable to infer that the 2D layered MoS₂/g-C₃N₄ provides a favorable support to graft CeO₂ NCs, and the formed heterostructures may accelerate the charge separation and generate more reactive sites via the coupling effect of CeO₂, MoS₂, and g-C₃N₄, which were investigated in detail as followed.

The interfacial effects and elemental valence states of pure CeO₂, MoS₂, g-C₃N₄, and CeO₂@MoS₂/g-C₃N₄ were analyzed by XPS. The high-resolution Mo 3d spectra (Fig. 3a) reveals that the peaks of Mo⁶⁺ 3d_{5/2}, Mo⁴⁺ 3d_{5/2}, and Mo⁴⁺ 3d_{3/2} are located at the binding energy (B.E.) of 238.2, 231.1, and 234.3 eV, respectively, which can be assigned to Mo⁴⁺/Mo⁶⁺ species in molybdenum [41]. Another peak at 228.5 eV matches well with the B.E. of S 2s. In the S 2p region (Fig. 3b), the spectra can be divided into two peaks centered at 164.2 and 165.5 eV, corresponding to S 2p_{3/2} and S 2p_{1/2}, respectively [42]. As depicted in Fig. 3c, the N 1s core level spectrum can be deconvoluted into three strong peaks, including 398.4 eV for C=N=C, 399.0 eV for N-(C)₃, and 400.5 eV for C=N-H [43,44]. Fig. 3d displays two fitted peaks at 284.8 and 288.2 eV from XPS spectrum of C 1s separately associated with C-C and N-C=N of g-C₃N₄. Moreover, it is obvious that after deconvolution, the Ce 3d spectrum (Fig. 3e) reflects two multiplets (i.e., 3d_{5/2} and 3d_{3/2}). Thereinto, the B.E. peaks of Ce 3d⁹4f²Lⁿ⁻¹ (882.7 eV) and Ce 3d⁹4f¹Lⁿ (885.1 eV) are denoted as v_0 and v' , respectively, belonging to Ce³⁺ 3d_{5/2}. As for Ce⁴⁺ 3d_{5/2}, Ce 3d⁹4f²Lⁿ⁻² (882.7 eV), Ce 3d⁹4f¹Lⁿ⁻¹ (889.0 eV), and Ce 3d⁹4f⁰Lⁿ (898.7 eV) correspond to v , v'' , and v''' [45]. Similarly, other peaks labelled as u_0 , u , u' , u'' , and u''' can be attributed to Ce 3d_{3/2}. Hence, the XPS results suggest that the Ce species are formed by a mixed valence states of Ce³⁺ and Ce⁴⁺, which is beneficial for the redox process in photocatalytic reaction [46]. The O 1s region in Fig. 3f is asymmetric, suggesting the presence of at least two types of oxygen species. The strong peak O' located at B.E. of 529.8 eV is due to lattice oxygen of CeO₂, and the weak peak O'' at B.E. of 531.9 eV originates from surface chemisorbed oxygen [47]. Interestingly, the B.E. of Mo 3d and S 2p in the

hybrids shifts to lower values, while the typical peaks of those Ce 3d, O 1s, C 1s, and N 1s shift to the higher B.E. in the XPS spectra. The decrease in B.E. normally accounts for a lower valence state with enhanced electron density [48,49]. Thus, the interfacial interaction of CeO₂@MoS₂/g-C₃N₄ lead to the electron transfer from g-C₃N₄ or CeO₂ to MoS₂, implying that the built-in electric fields are formed among the three moieties in the heterostructure.

3.2. Bandgap structure analysis

Fig. 4a exhibits the UV-vis DRS of the ternary composites of CeO₂@MoS₂/g-C₃N₄ along with binary composites and single components. The absorption edges of bare CeO₂ and g-C₃N₄ are estimated to be approximately 420 and 460 nm, respectively, and CeO₂/g-C₃N₄ displays a slight red-shift compared to g-C₃N₄. After loading black MoS₂ cocatalyst, the light absorption in the visible light region (440–800 nm) of the hybrids increases significantly, thus the hybrids can absorb more photons for photocatalytic reactions [50]. Additionally, the bandgap energies of MoS₂, g-C₃N₄, and CeO₂ were estimated by the Tauc's equation ($ahv = A(hv - E_g)^{n/2}$), where a , h , v , and E_g referred to absorption coefficient, Planck constant, light frequency, and band gap energy, respectively; n depends on the properties of the transition, i.e., direct transition (MoS₂, $n = 1$) and indirect transition (g-C₃N₄, CeO₂, $n = 4$) [29,51]. Consequently, the E_g values are calculated, i.e., 1.81, 2.69, and 3.06 eV for MoS₂, g-C₃N₄, and CeO₂ (Fig. 4b), respectively. Besides, the valence band maximum (VBM) is also determined in the XPS valence spectra (Fig. 4c). Based on the equation of $E_{CB} = E_{VB} - E_g$, the conduction band minimum (CBM) can be determined to be -0.49 eV for CeO₂, -1.07 eV for g-C₃N₄, and -0.13 eV for MoS₂.

3.3. Charge transfer properties

PL emission is originated from the radiative recombination of electron-hole pairs, which can be used to evaluate the charge transfer and separation of the as-prepared heterojunctions [52,53]. Fig. 5a depicts that pristine g-C₃N₄ shows an extremely intense PL signal with the emission band centered at around 470 nm under 325 nm laser excitation, which can be ascribed to its rapid charge recombination [54]. A slightly reduced emission peak is observed for the physical mixture of CeO₂@MoS₂/g-C₃N₄ (CMg-PM) due to the poor interactions among the components in the mechanical mixture. Furthermore, the PL intensities of g-C₃N₄-based heterojunctions dramatically decreased, especially for the ternary composite of CeO₂@MoS₂/g-C₃N₄, suggesting the enhanced separation efficiency and suppressed recombination of charge carriers at the interfaces.

To gain deeper insight into the behavior of the photogenerated electrons and holes, the transient photocurrent responses of g-C₃N₄, MoS₂/g-C₃N₄, CeO₂/g-C₃N₄, and CeO₂@MoS₂/g-C₃N₄ electrodes were

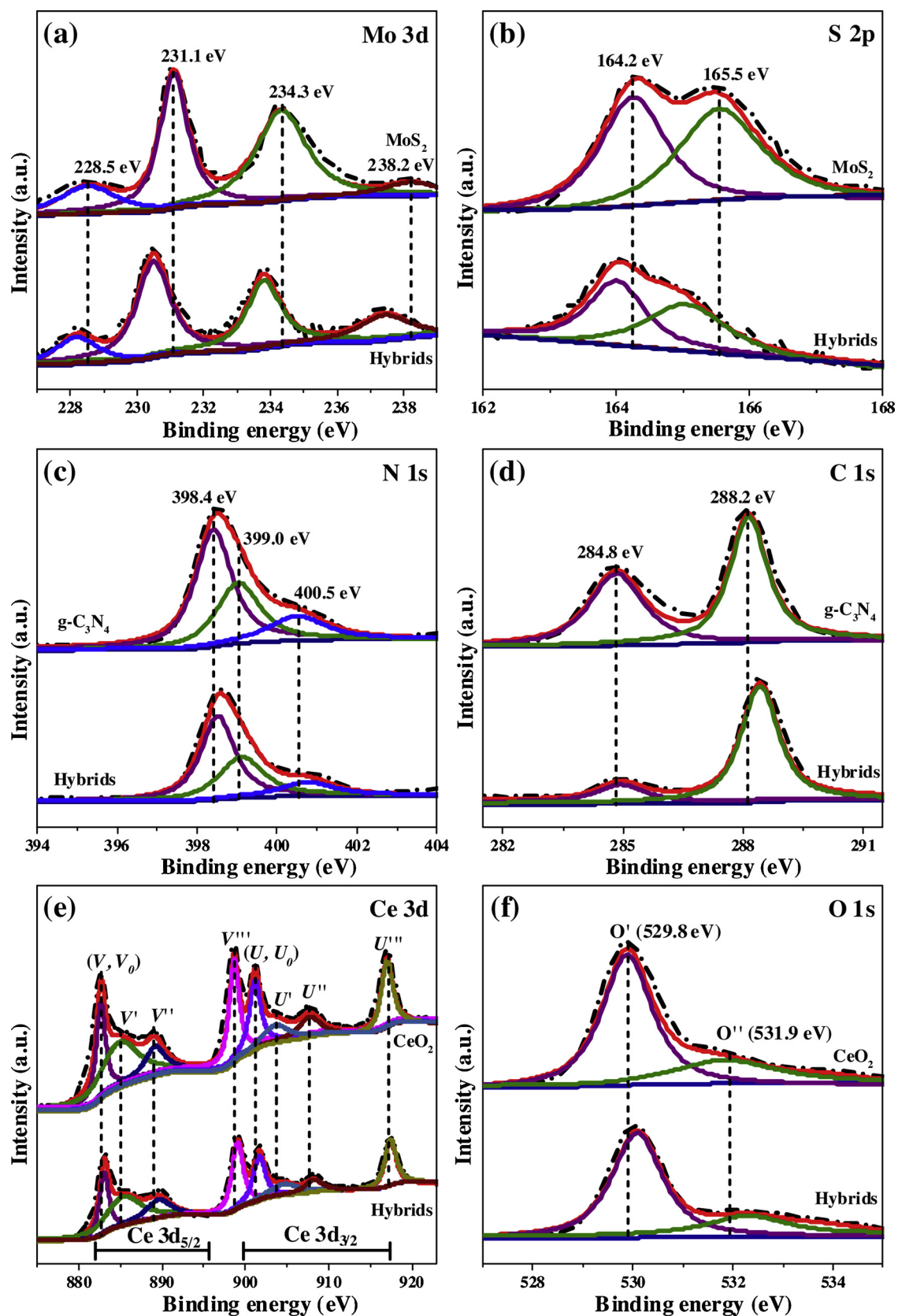


Fig. 3. High-resolution XPS spectra of (a) Mo 3d, (b) S 2p, (c) N 1s, (d) C 1s, (e) Ce 3d, and (f) O 1s for MoS₂, g-C₃N₄, CeO₂, and CeO₂@MoS₂/g-C₃N₄.

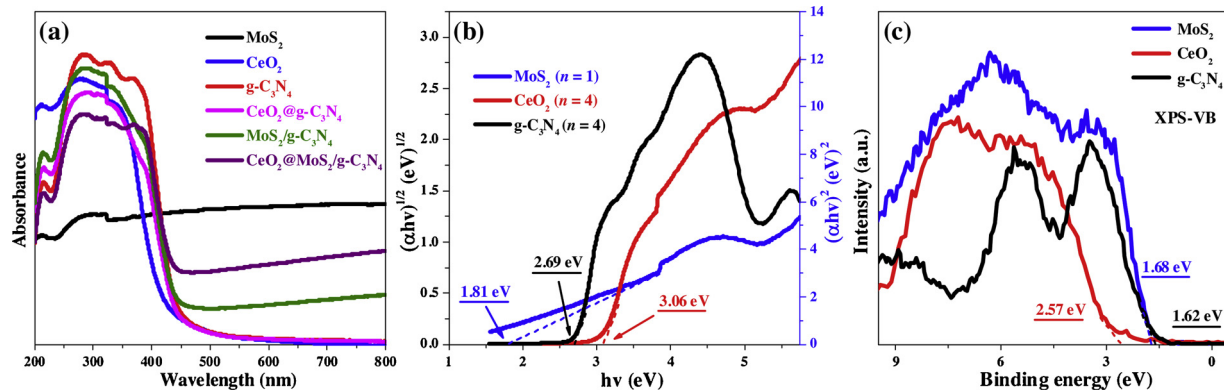


Fig. 4. (a) UV-vis DRS of all photocatalysts. (b) Plot of $(\alpha h\nu)^2$ and $(\alpha h\nu)^1/2$ versus photon energy, and (c) valence-band XPS spectra of CeO₂, g-C₃N₄, and MoS₂.

recorded for several on-off cycles in Fig. 5b. In general, the higher photocurrent intensity suggests the generation of large amounts of charge carriers as well as their efficient separation and transportation [55,56]. As expected, once CeO₂@MoS₂/g-C₃N₄ was spin-coated onto the bare ITO, the corresponding photocurrent was sharply increased to 0.89 μA, which is about 2.5, 1.8, and 1.4 times higher than g-C₃N₄ (0.36 μA), CeO₂@g-C₃N₄ (0.49 μA), and MoS₂/g-C₃N₄ (0.64 μA), respectively. These results are in agreement with the PL observation, confirming that the heterostructure effectively facilitates the electron-hole separation and transport process.

3.4. H₂O reactant adsorption

For photocatalytic water splitting, the adsorption ability of reactant H₂O molecule on the photocatalyst is a crucial step and worthy of investigation [57]. On the basis of that, the hydrophilic property of the obtained CeO₂@MoS₂/g-C₃N₄ was studied by the contact-angle and FT-IR measurements. The contact-angle of MoS₂/g-C₃N₄ and CeO₂@MoS₂/g-C₃N₄ samples were conducted for 4 times, and the corresponding results are listed in Table S2. Clearly, the four tests of MoS₂/g-C₃N₄ (Fig. S3a-d) exhibit the contact angles of 32.7°, 33.8°, 32.8°, and 31.9°, respectively, indicating mediocre hydrophilicity of the surface [58,59]. After the decoration with CeO₂, the values of the contact angle over CeO₂@MoS₂/g-C₃N₄ heterojunction apparently descend to 26.7°, 26.0°, 27.7°, and 25.6° (Fig. S3e-h), elucidating that the ternary composite possesses better hydrophilicity than MoS₂/g-C₃N₄, which is favorable for the reactant H₂O adsorption. Thereinto, 32.7° (Fig. 6a) and 26.7°

(Fig. 6b) are close to the average values, and thus were chosen as the representative values. Moreover, the surface functional groups of photocatalyst were analyzed by FT-IR in Fig. 6c. Typically, the broad absorption centered at 3600–3000 cm⁻¹ arises from the stretching vibration of hydroxyl groups of surface adsorbed H₂O molecules, and the peaks in the range of 1700–800 cm⁻¹ are the typical stretching vibrations of g-C₃N₄ [60]. Compared with the monomers and binary composites, the relative peak intensity of hydroxyl group in the s-triazine ring system is stronger in the CeO₂@MoS₂/g-C₃N₄ ternary composite, which further verifies that the water molecules are more prone to be adsorbed on the CeO₂@MoS₂/g-C₃N₄, and subsequently its accessible surface is beneficial for reducing the energy barrier in water splitting.

As is well known, Ce³⁺ species with 4f¹ electron is more helpful for the adsorption of water molecules [61]. Therefore, we performed EPR analysis of the solid samples (Fig. 6d). Similar to the results of XPS-Ce 3d, the ESR signal at $g = 1.96$ is attributed to Ce³⁺ [62]. The signal intensities are in an order of CeO₂@MoS₂/g-C₃N₄ > CeO₂/g-C₃N₄ > CeO₂, implying that due to the intensive interfacial interaction, more Ce³⁺ species generated in the CeO₂@MoS₂/g-C₃N₄ heterojunction and then more active sites formed for H₂O molecules adsorption. Hence, combined with the results of the contact-angle, FT-IR and EPR, it can be reasonably deduced that the adsorption of reactant H₂O molecules surrounding the surface-reactive sites is enhanced on CeO₂@MoS₂/g-C₃N₄, and the decreased adsorption energy may promote the photocatalytic water splitting.

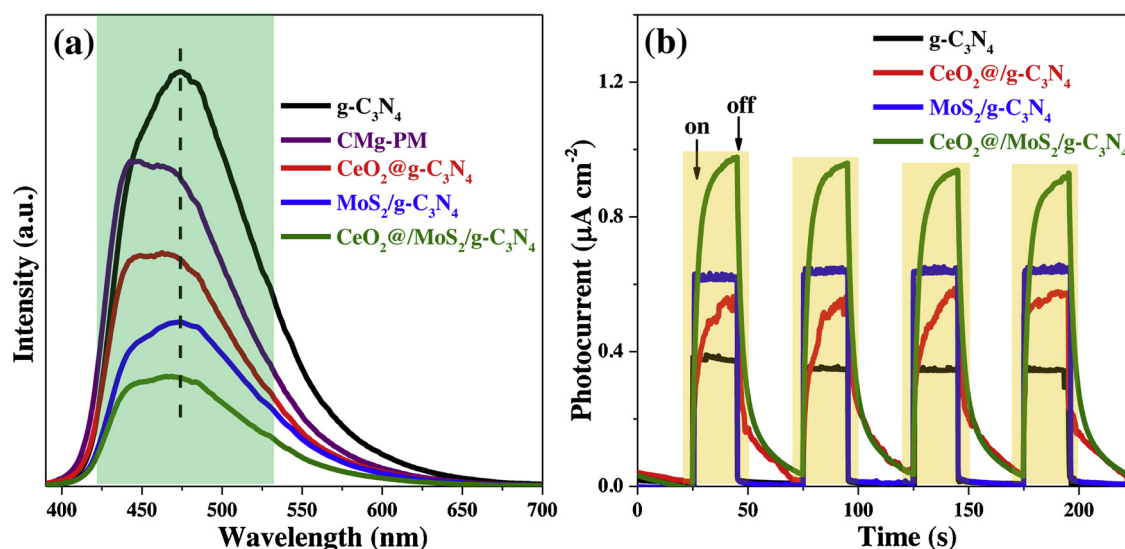


Fig. 5. Steady-state PL spectra (a) and transient photocurrent responses (b) of as-prepared photocatalysts.

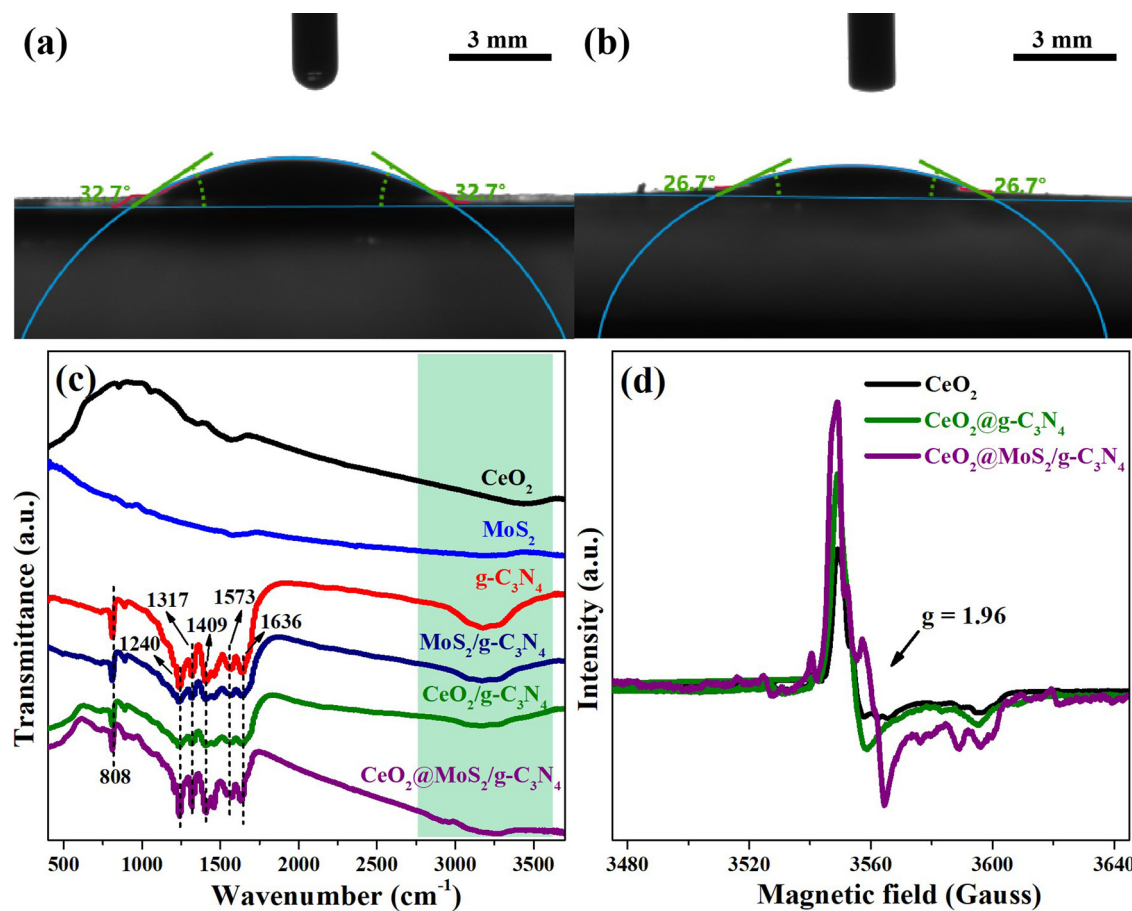


Fig. 6. Contact angle measurements of (a) MoS₂/g-C₃N₄ and (b) CeO₂@MoS₂/g-C₃N₄. FTIR spectra (c) and (d) EPR spectra of different samples.

3.5. H₂ evolution activity and possible mechanism

The photocatalytic performances of the catalysts for H₂ evolution were evaluated in the presence of Na₂S (0.5 M) and Na₂SO₃ (0.5 M) as the sacrificial reagents under visible light irradiation. There is no evolution of H₂ in the reference experiment without either photocatalyst or irradiation. Fig. 7a and b display the profiles of H₂ production and H₂ evolution rate (HER) of different samples within 4 h. No appreciable H₂ was generated for MoS₂. Low HER of 3.7 μmol/h and 7.9 μmol/h were separately detected for CeO₂ and g-C₃N₄ because of the fast electron-hole recombination or high kinetic barrier [63]. Notably, compared with CeO₂/g-C₃N₄, MoS₂/g-C₃N₄, and physical mixture of three moieties (CMg-PM), the ternary composite of CeO₂@MoS₂/g-C₃N₄ achieves the highest HER of 65.4 μmol/h, which is greater than previous reports (Table S3). This can be attributed to the synergistic effects of the optimized optical/electronic properties and decreased energy threshold of H₂O adsorption arising from the communicated electric fields among their single components. Moreover, a slight decrease of HER over CeO₂@MoS₂/g-C₃N₄ can be observed during 3 consecutive cycles in Fig. 7c. However, no obvious decrease in HER was found even for the catalysts which had been stored for 12 weeks, validating its impressive stability. The XRD (Fig. S4a) and XPS (Fig. S4b) results of CeO₂@MoS₂/g-C₃N₄ exhibited that no noticeable changes in its characteristic lines, indicating the stability for multiple runs. In addition, the dependence of external quantum efficiency (QE) on the wavelength corroborates the light absorption behavior of CeO₂@MoS₂/g-C₃N₄ in Fig. 7d. The corresponding external QE was tested to be 10.35% at $\lambda = 420$ nm, which is even higher than most of the previously reported photocatalysts (Table S3), demonstrating the efficient utilization of photogenerated charges [64]. The external QE remarkably decreased as light wavelength was prolonged, achieving 5.82%, 0.79%, and 0.06% at 435, 485,

and 520 nm, respectively, implying that the CeO₂@MoS₂/g-C₃N₄ heterojunction still converts solar energy for photocatalytic H₂ production under monochromatic visible light ($\lambda > 420$ nm).

On the basis of the above experimental results and analysis, a tentative mechanism was proposed in Fig. 8 for the superior H₂ evolution activity over CeO₂@MoS₂/g-C₃N₄ heterojunction. The outstanding photocatalytic activity arose from the following factors:

- Driven by the inner electric fields and well-matched energy band structures, the stronger electronic interactions on CeO₂@MoS₂/g-C₃N₄ interfaces facilitated the photogenerated electrons to transfer from the CB of MoS₂ to the VB of g-C₃N₄. Meanwhile, the electrons in the VB of g-C₃N₄ (1.62 V vs NHE) are excited to its CB (-1.07 V vs NHE) under the visible light exposure, and then directly migrate to the lower CB of CeO₂ (-0.49 V vs NHE). Therefore, such a ternary system induces consecutive multi-step electron transfer, which efficiently accelerates the interfacial charge transport and separation.
- The accumulated holes on g-C₃N₄ result in the partial oxidation of Ce³⁺ to Ce⁴⁺ (Ce³⁺/Ce⁴⁺ reversibility pairs), which plays a crucial role in prolonging the lifetime of photoinduced charge carriers. In this process, Ce⁴⁺ species are capable of trapping the electrons at the interface to restrain the electron-hole recombination. Notably, Ce³⁺/oxygen vacancies can preserve their strong reducibility and provide abundant adsorption sites to the reactant H₂O molecules, hereby decreasing the H₂O adsorption energy and promoting the photocatalytic water splitting to H₂.
- The hybridization with MoS₂ significantly broadens the visible light absorption and reduces the reflection of light, enabling the formation of more free carriers in photocatalytic water splitting. Meanwhile, the layered 2D/2D architectures of MoS₂ cocatalyst

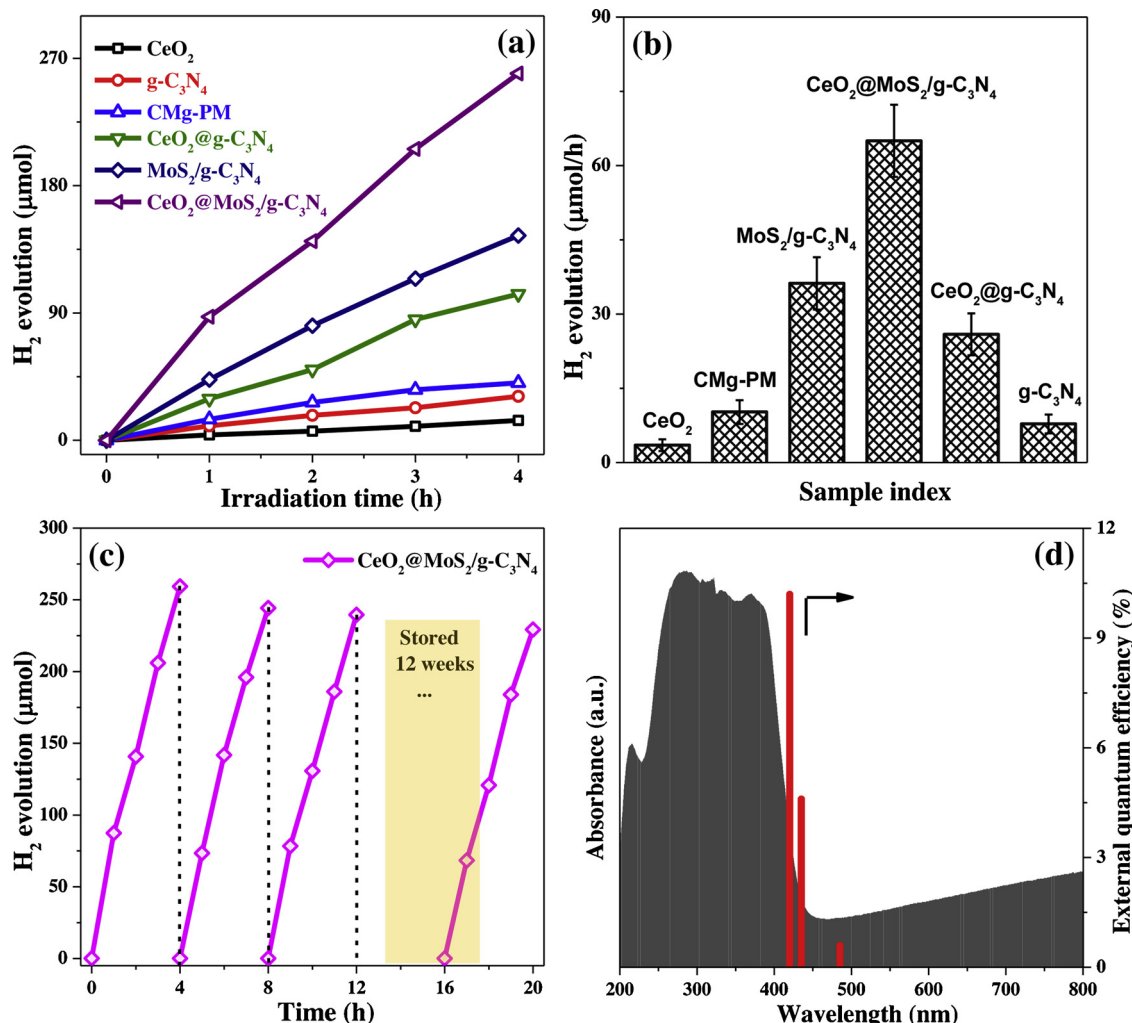


Fig. 7. (a) Time courses of photocatalytic H₂ production and (b) average HER of CeO₂, g-C₃N₄, CeO₂@g-C₃N₄, MoS₂/g-C₃N₄, and CeO₂@MoS₂/g-C₃N₄ under visible light exposure. (c) Recycling H₂ evolution texts and (d) wavelength-dependent external QE over CeO₂@MoS₂/g-C₃N₄.

and g-C₃N₄ NSs not only provide abundant accessible sites for catalysis and anchoring CeO₂ NCs, but also shorten the distance of mass and charge transfer.

Integrating with the advantages of single components of CeO₂, MoS₂, and g-C₃N₄, the elaborately desired CeO₂@MoS₂/g-C₃N₄

heterostructure facilitates multi-step electron transfer at intimate interfaces and yields more adsorption of reactant H₂O molecule. Hence, the H₂ evolution activity is impressively boosted due to the improved visible light adsorption, faster charge separation, and more surface-reactive sites.

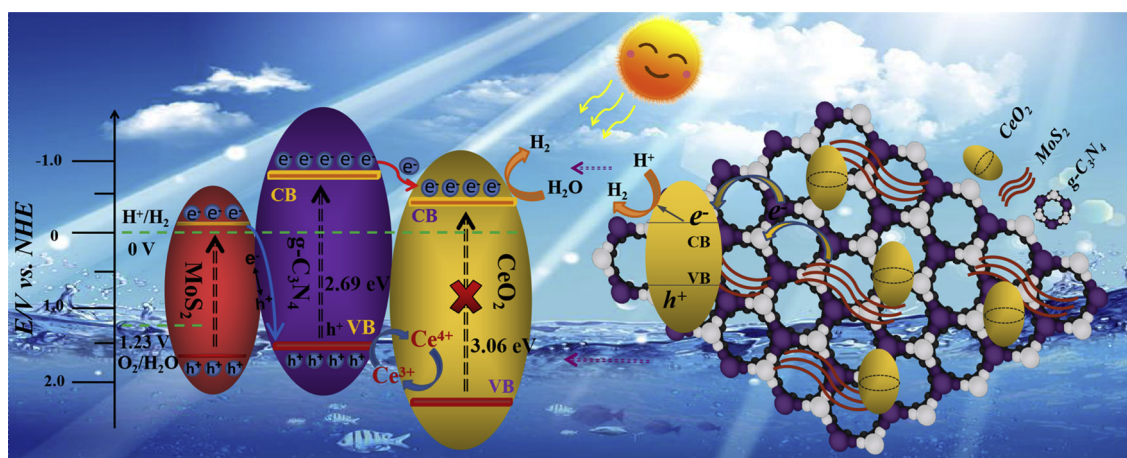


Fig. 8. Schematic diagram of the multistep charge-transfer processes for photocatalytic H₂ evolution from water splitting over CeO₂@MoS₂/g-C₃N₄.

4. Conclusions

In summary, a facile strategy was developed to fabricate CeO_2 @ MoS_2 / $\text{g-C}_3\text{N}_4$ composite with 0D CeO_2 NCs grown on the surface of 2D MoS_2 / $\text{g-C}_3\text{N}_4$ NSs. Such heterojunctions endowed a relatively short diffusion distance for faster charge transfer, more $\text{Ce}^{3+}/\text{Ce}^{4+}$ reversibility pairs for reduced electron-hole recombination and decreased H_2O adsorption energy, as well as available abundant active sites for water splitting. The optimized ternary 0D-2D composite of CeO_2 @ MoS_2 / $\text{g-C}_3\text{N}_4$ established a system with short-distance electron transport and multi-step electron transfer. As a result, the photocatalytic system exhibited enhanced H_2 production activity (65.4 $\mu\text{mol}/\text{h}$) with a high external QE of 10.35% at 420 nm, compared to those of the binary composites and pristine components. This work presents an effective and economical strategy to design a novel 0D-2D photocatalytic system for efficient H_2 evolution without noble metals.

Declaration of Competing Interest

The authors declare that they have no known competing financial interests or personal relationships that could have appeared to influence the work reported in this paper.

Acknowledgements

The authors gratefully acknowledge the financial support from the National Natural Science Foundation of China (Grant 21876078, 21707066), Major Science and Technology Program for Water Pollution Control and Treatment (2017ZX07204004), Jiangsu Key R&D Plan (BE2017711), Environmental Monitoring Fund of Jiangsu Province (1801) and the Scientific Research Foundation of Graduate School of Nanjing University (2018CL01).

Appendix A. Supplementary data

Supplementary material related to this article can be found, in the online version, at doi:<https://doi.org/10.1016/j.apcatb.2019.118072>.

References

- [1] H. Yamashita, K. Mori, Y. Kuwahara, T. Kamegawa, M.C. Wen, P. Verma, M. Che, Single-site and nano-confined photocatalysts designed in porous materials for environmental uses and solar fuels, *Chem. Soc. Rev.* 47 (2018) 8072–8096.
- [2] K. Mori, K. Miyawaki, H. Yamashita, Ru and Ru-Ni nanoparticles on TiO_2 support as extremely active catalysts for hydrogen production from ammonia–borane, *ACS Catal.* 6 (2016) 3128–3135.
- [3] Z.F. Jiang, B. Wang, J.C. Yu, J.F. Wang, T.C. An, H.J. Zhao, H.M. Li, S.Q. Yuan, P.K. Wong, $\text{AgInS}_2/\text{In}_2\text{S}_3$ heterostructure sensitization of *Escherichia coli* for sustainable hydrogen production, *Nano Energy* 46 (2018) 234–240.
- [4] S.N. Xiao, P.J. Liu, W. Zhu, G.S. Li, D.Q. Zhang, H.X. Li, Copper nanowires: a substitute for noble metals to enhance photocatalytic H_2 generation, *Nano Lett.* 15 (2015) 4853–4858.
- [5] W.J. Jiang, W.J. Luo, R.L. Zong, W.Q. Yao, Z.P. Li, Y.F. Zhu, Polyaniline/carbon nitride nanosheets composite hydrogel: a separation-free and high-efficient photocatalyst with 3D hierarchical structure, *Small* 12 (2016) 4370–4378.
- [6] J.J. Kong, G.Y. Li, M.C. Wen, J.Y. Chen, H.L. Liu, T.C. An, The synergic degradation mechanism and photothermocatalytic mineralization of typical VOCs over Pt/CeO_2 ordered porous catalysts under simulated solar irradiation, *J. Catal.* 370 (2019) 88–96.
- [7] X.J. Yao, Y. Xiong, W.X. Zou, L. Zhang, S.G. Wu, X. Dong, F. Gao, Y. Deng, C.J. Tang, Z. Chen, L. Dong, Y. Chen, Correlation between the physicochemical properties and catalytic performances of $\text{Ce}_x\text{Sn}_{1-x}\text{O}_2$ mixed oxides for NO reduction by CO , *Appl. Catal. B* 144 (2014) 152–165.
- [8] L.J. Xu, J.L. Wang, Magnetic nanoscaled $\text{Fe}_3\text{O}_4/\text{CeO}_2$ composite as an efficient Fenton-like heterogeneous catalyst for degradation of 4-chlorophenol, *Environ. Sci. Technol.* 46 (2012) 10145–10153.
- [9] S. Mansingh, D.K. Padhi, K.M. Parida, Enhanced visible light harnessing and oxygen vacancy promoted N, S co-doped CeO_2 nanoparticle: a challenging photocatalyst for Cr(VI) reduction, *Catal. Sci. Technol.* 7 (2017) 2772–2781.
- [10] A. Nozaki, T. Yasuoka, Y. Kuwahara, T. Ohmichi, K. Mori, T. Nagase, H.Y. Yasuda, H. Yamashita, Oxidation of benzyl alcohol over nanoporous Au/CeO_2 catalysts prepared from amorphous alloys and effect of alloying Au with amorphous alloys, *Ind. Eng. Chem. Res.* 57 (2018) 5599–5605.
- [11] Y. Okamoto, S. Ida, J. Hyodo, H. Hagiwara, T. Ishihara, Synthesis and photocatalytic activity of rhodium-doped calcium niobate nanosheets for hydrogen production from a water/methanol system without cocatalyst loading, *J. Am. Chem. Soc.* 133 (2011) 18034–18037.
- [12] Y.Y. Wang, W.J. Jiang, W.J. Luo, X.J. Chen, Y.F. Zhu, Ultrathin nanosheets $\text{g-C}_3\text{N}_4$ @ Bi_2WO_6 core-shell structure via low temperature reassembled strategy to promote photocatalytic activity, *Appl. Catal. B* 237 (2018) 633–640.
- [13] J.W. Fu, J.G. Yu, C.J. Jiang, B. Cheng, $\text{g-C}_3\text{N}_4$ -based heterostructured photocatalysts, *Adv. Energy Mater.* 8 (2018) 1701503.
- [14] G.S. Li, Z.C. Lian, W.C. Wang, D.Q. Zhang, H.X. Li, Nanotube-confinement induced size-controllable $\text{g-C}_3\text{N}_4$ quantum dots modified single-crystalline TiO_2 nanotube arrays for stable synergistic photoelectrocatalysis, *Nano Energy* 19 (2016) 446–454.
- [15] Z.J. Xie, Y.P. Feng, F.L. Wang, D.N. Chen, Q.X. Zhang, Y.Q. Zeng, W.Y. Lv, G.G. Liu, Construction of carbon dots modified $\text{MoO}_3/\text{g-C}_3\text{N}_4$ Z-scheme photocatalyst with enhanced visible-light photocatalytic activity for the degradation of tetracycline, *Appl. Catal. B* 229 (2018) 96–104.
- [16] F.L. Wang, Y.F. Wang, Y.P. Feng, Y.Q. Zeng, Z.J. Xie, Q.X. Zhang, Y.H. Su, P. Chen, Y. Liu, K. Yao, W.Y. Lv, G.G. Liu, Novel ternary photocatalyst of single atom-dispersed silver and carbon quantum dots co-loaded with ultrathin $\text{g-C}_3\text{N}_4$ for broad spectrum photocatalytic degradation of naproxen, *Appl. Catal. B* 221 (2018) 510–520.
- [17] Y.J. Yuan, Y. Yang, Z.J. Li, D.Q. Chen, S.T. Wu, G.L. Fang, W.F. Bai, M.Y. Ding, L.X. Yang, D.P. Cao, Z.T. Yu, Z.G. Zou, Promoting charge separation in $\text{g-C}_3\text{N}_4$ /graphene/ MoS_2 photocatalysts by two-dimensional nanojunction for enhanced photocatalytic H_2 production, *ACS Appl. Energy Mater.* 1 (2018) 1400–1407.
- [18] Y.Z. Liu, H.Y. Zhang, J. Ke, J.Q. Zhang, W.J. Tian, X.Y. Xu, X.G. Duan, H.Q. Sun, M.O. Tade, S.B. Wang, 0D (MoS_2)/2D ($\text{g-C}_3\text{N}_4$) heterojunctions in Z-scheme for enhanced photocatalytic and electrochemical hydrogen evolution, *Appl. Catal. B* 228 (2018) 64–74.
- [19] F.L. Wang, P. Chen, Y.P. Feng, Z.J. Xie, Y. Liu, Y.H. Su, Q.X. Zhang, Y.F. Wang, K. Yao, W.Y. Lv, G.G. Liu, Facile synthesis of N-doped carbon dots/ $\text{g-C}_3\text{N}_4$ photocatalyst with enhanced visible-light photocatalytic activity for the degradation of indomethacin, *Appl. Catal. B* 207 (2017) 103–113.
- [20] C.Z. Zhu, X. Chen, J. Ma, C. Gu, Q.M. Xian, T.T. Gong, C. Sun, Carbon nitride-modified defective TiO_{2-x} -@carbon spheres for photocatalytic H_2 evolution and pollutants removal: synergistic effect and mechanism insight, *J. Phys. Chem. C* 122 (2018) 20444–20458.
- [21] G.Y. Li, X. Nie, J.Y. Chen, Q. Jiang, T.C. An, P.K. Wong, H.M. Zhang, H.J. Zhao, H. Yamashita, Enhanced visible-light-driven photocatalytic inactivation of *Escherichia coli* using $\text{g-C}_3\text{N}_4/\text{TiO}_2$ hybrid photocatalyst synthesized using a hydrothermal-calcination approach, *Water Res.* 86 (2015) 17–24.
- [22] D.L. Jiang, J. Li, C.S. Xing, Z.Y. Zhang, S.C. Meng, M. Chen, Two-dimensional $\text{CaIn}_2\text{S}_4/\text{g-C}_3\text{N}_4$ heterojunction nanocomposite with enhanced visible-light photocatalytic activities: interfacial engineering and mechanism insight, *ACS Appl. Mater. Interfaces* 7 (2015) 19234–19242.
- [23] H.P. Li, W.G. Hou, N. Du, R.J. Zhang, X.T. Tao, Synthesis and characterization of $\text{g-C}_3\text{N}_4/\text{Bi}_2\text{MoO}_6$ heterojunctions with enhanced visible light photocatalytic activity, *Appl. Catal. B* 160 (2014) 89–97.
- [24] Q.Z. Xiong, Y. Wang, P.F. Liu, L.R. Zheng, G.Z. Wang, H.G. Yang, P.K. Wong, H.M. Zhang, H.J. Zhao, Cobalt covalent doping in MoS_2 to induce bifunctionality of overall water splitting, *Adv. Mater.* 30 (2018) 1801450.
- [25] G. Swain, S. Sultana, B. Naik, K. Parida, Coupling of crumpled-type novel MoS_2 with CeO_2 nanoparticles: a noble-metal-free p–n heterojunction composite for visible-light photocatalytic H_2 production, *ACS Omega* 2 (2017) 3745–3753.
- [26] J. Yan, Z.G. Chen, H.Y. Ji, Z. Liu, X. Wang, Y.G. Xu, X.J. She, L.Y. Huang, L. Xu, H. Xu, H.M. Li, Construction of a 2D graphene-like $\text{MoS}_2/\text{C}_3\text{N}_4$ heterojunction with enhanced visible-light photocatalytic activity and photoelectrochemical activity, *Chem. Eur. J.* 22 (2016) 4764–4773.
- [27] Q.Z. Xiong, X. Zhang, H.J. Wang, G.Q. Liu, G.Z. Wang, H.M. Zhang, H.J. Zhao, One-step synthesis of cobalt-doped MoS_2 nanosheets as bifunctional electrocatalysts for overall water splitting under both acidic and alkaline conditions, *Chem. Commun.* 54 (2018) 3859–3862.
- [28] Q. Han, B. Wang, J. Gao, Z.H. Cheng, Y. Zhao, Z.P. Zhang, L.T. Qu, Atomically thin mesoporous nanomesh of graphitic C_3N_4 for high-efficiency photocatalytic hydrogen evolution, *ACS Nano* 10 (2016) 2745–2751.
- [29] Y.Z. Liu, X.Y. Xu, J.Q. Zhang, H.Y. Zhang, W.J. Tian, X.J. Li, M.O. Tade, H.Q. Sun, S.B. Wang, Flower-like MoS_2 on graphitic carbon nitride for enhanced photocatalytic and electrochemical hydrogen evolutions, *Appl. Catal. B* 239 (2018) 334–344.
- [30] X.W. Shi, M. Fujitsuka, S. Kim, T. Majima, Faster electron injection and more active sites for efficient photocatalytic H_2 evolution in $\text{g-C}_3\text{N}_4/\text{MoS}_2$ hybrid, *Small* 14 (2018) 1703277.
- [31] D.J. Martin, K.P. Qiu, S.A. Shevlin, A.D. Handoko, X.W. Chen, Z.X. Guo, J.W. Tang, Highly efficient photocatalytic H_2 evolution from water using visible light and structure-controlled graphitic carbon nitride, *Angew. Chem. Int. Ed.* 53 (2014) 9240–9245.
- [32] B. Hu, C.P. Cai, T.J. Chen, M.S. Fan, C.J. Song, X. Yan, W.D. Shi, Hydrothermal synthesis $\text{g-C}_3\text{N}_4/\text{nano-InVO}_4$ nanocomposites and enhanced photocatalytic activity for hydrogen production under visible light irradiation, *ACS Appl. Mater. Interfaces* 7 (2015) 18247–18256.
- [33] Y. Hou, Z.H. Wen, S.M. Cui, X.R. Guo, J.H. Chen, Constructing 2D porous graphitic C_3N_4 nanosheets/nitrogen-doped graphene/layered MoS_2 ternary nanojunction with enhanced photoelectrochemical activity, *Adv. Mater.* 25 (2013) 6291–6297.
- [34] R. Si, M. Flytzani-Stephanopoulos, Shape and crystal-plane effects of nanoscale ceria on the activity of Au/CeO_2 catalysts for the water-gas shift reaction, *Angew. Chem. Int. Ed.* 47 (2008) 2884–2887.

[35] C.Z. Zhu, T. Gong, Q.M. Xian, J.M. Xie, Graphite-like carbon nitride coupled with tiny Bi_2S_3 nanoparticles as 2D/0D heterojunction with enhanced photocatalytic activity, *Appl. Surf. Sci.* 444 (2018) 75–86.

[36] X.Y. Gong, Y.Q. Gu, N. Li, H.Y. Zhao, C.J. Jia, Y.P. Du, Thermally stable hierarchical nanostructures of ultrathin MoS_2 nanosheet-coated CeO_2 hollow spheres as catalyst for ammonia decomposition, *Inorg. Chem.* 55 (2016) 3992–3999.

[37] Y.C. Huang, Y.R. Lu, Y. Lin, Y.C. Mao, G.F. Ouyang, H. Liu, S.Q. Zhang, Y.X. Tong, Cerium-based hybrid nanorods for synergistic photo-thermocatalytic degradation of organic pollutants, *J. Mater. Chem. A* 6 (2018) 24740–24747.

[38] Q. Li, N. Zhang, Y. Yang, G.Z. Wang, D.H.L. Ng, High efficiency photocatalysis for pollutant degradation with $\text{MoS}_2/\text{C}_3\text{N}_4$ heterostructures, *Langmuir* 30 (2014) 8965–8972.

[39] X.D. Li, Y. Feng, M.C. Li, W. Li, H. Wei, D.D. Song, Smart hybrids of Zn_2GeO_4 nanoparticles and ultrathin $\text{g-C}_3\text{N}_4$ layers: synergistic lithium storage and excellent electrochemical performance, *Adv. Funct. Mater.* 25 (2015) 6858–6866.

[40] C.Z. Zhu, Y.T. Wang, Z.F. Jiang, A.N. Liu, Y. Pu, Q.M. Xian, W.X. Zou, C. Sun, Ultrafine Bi_2TaO_7 nanodot-decorated V, N codoped TiO_2 nanoblocks for visible-light photocatalytic activity: Interfacial effect and mechanism insight, *ACS Appl. Mater. Interfaces* 11 (2019) 13011–13021.

[41] Y.C. Lin, W.J. Zhang, J.K. Huang, K.K. Liu, Y.H. Lee, C.T. Liang, C.W. Chu, L.J. Li, Wafer-scale MoS_2 thin layers prepared by MoO_3 sulfurization, *Nanoscale* 4 (2012) 6637–6641.

[42] W.J. Zhou, Z.Y. Yin, Y.P. Du, X. Huang, Z.Y. Zeng, Z.X. Fan, H. Liu, J.Y. Wang, H. Zhang, Synthesis of few-layer MoS_2 nanosheet-coated TiO_2 nanobelts heterostructures for enhanced photocatalytic activities, *Small* 9 (2013) 140–147.

[43] Z.F. Jiang, W.M. Wang, H.M. Li, S.Q. Yuan, H.J. Zhao, P.K. Wong, A hierarchical Z-scheme $\alpha\text{-Fe}_2\text{O}_3/\text{g-C}_3\text{N}_4$ hybrid for enhanced photocatalytic CO_2 reduction, *Adv. Mater.* 30 (2018) 1706108.

[44] T.Y. Ma, S. Dai, M. Jaroniec, S.Z. Qiao, Graphitic carbon nitride nanosheet–carbon nanotube three-dimensional porous composites as high-performance oxygen evolution electrocatalysts, *Angew. Chem. Int. Ed.* 53 (2014) 7281–7285.

[45] X.J. Yao, L. Chen, J. Cao, F.M. Yang, W. Tan, L. Dong, Morphology and crystal-plane effects of CeO_2 on $\text{TiO}_2/\text{CeO}_2$ catalysts during $\text{NH}_3\text{-SCR}$ reaction, *Ind. Eng. Chem. Res.* 57 (2018) 12407–12419.

[46] M.E. Khan, M.M. Khan, M.H. Cho, Ce^{3+} -ion, surface oxygen vacancy, and visible light-induced photocatalytic dye degradation and photocapacitive performance of CeO_2 -graphene nanostructures, *Sci. Rep.* 7 (2017) 5928.

[47] G. Grzybek, P. Stelmachowski, S. Gudkova, P. Indyka, Z. Sojka, N. Guillen-Hur-tado, V. Rico-Perez, A. Bueno-Lopez, A. Kotarba, Strong dispersion effect of cobalt spinel active phase spread over ceria for catalytic N_2O decomposition: the role of the interface periphery, *Appl. Catal. B* 180 (2016) 622–629.

[48] M.S. Zhu, Z.C. Sun, M. Fujitsuka, T. Majima, Z-Scheme photocatalytic water splitting on a 2D heterostructure of black phosphorus/bismuth vanadate using visible light, *Angew. Chem. Int. Ed.* 57 (2018) 2160–2164.

[49] X.X. Zhao, J.R. Feng, J.W. Liu, J. Lu, W. Shi, G.M. Yang, G.C. Wang, P.Y. Feng, P. Cheng, Metal-organic framework-derived ZnO/ZnS heteronanostructures for efficient visible-light-driven photocatalytic hydrogen production, *Adv. Sci.* 5 (2018) 1700590.

[50] T. Huang, Y.T. Luo, W. Chen, J.C. Yao, X.H. Liu, Self-assembled $\text{MoS}_2\text{-GO}$ framework as an efficient cocatalyst of CuInZnS for visible-light driven hydrogen evolution, *ACS Sustain. Chem. Eng.* 6 (2018) 4671–4679.

[51] L.Y. Zhu, H. Li, P.F. Xia, Z.R. Liu, D.H. Xiong, Hierarchical ZnO decorated with CeO_2 nanoparticles as the direct Z-scheme heterojunction for enhanced photocatalytic activity, *ACS Appl. Mater. Interfaces* 10 (2018) 39679–39687.

[52] W.P. Zhang, G.Y. Li, H.L. Liu, J.Y. Chen, S.T. Mao, T.C. An, Micro/nano-bubble assisted synthesis of $\text{Au}/\text{TiO}_2@\text{CNTs}$ composite photocatalyst for photocatalytic degradation of gaseous styrene and its enhanced catalytic mechanism, *Environ. Sci.: Nano* 6 (2019) 948–958.

[53] K. Mori, J. Aoyama, M. Kawashima, H. Yamashita, Visible-light driven H_2 production utilizing iridium and rhodium complexes intercalated into a zirconium phosphate layered matrix, *Dalton Trans.* 43 (2014) 10541–10547.

[54] K. Li, M. Han, R. Chen, S.L. Li, S.L. Xie, C.Y. Mao, X.H. Bu, X.L. Cao, L.Z. Dong, P.Y. Feng, Y.Q. Lan, Hexagonal@cubic CdS core@shell nanorod photocatalyst for highly active production of H_2 with unprecedented stability, *Adv. Mater.* 28 (2016) 8906–8911.

[55] Y.W. Feng, H. Li, L.L. Ling, S. Yan, D.L. Pan, H. Ge, H.X. Li, Z.F. Bian, Enhanced photocatalytic degradation performance by fluid-induced piezoelectric field, *Environ. Sci. Technol.* 52 (2018) 7842–7848.

[56] Y.C. Huang, K.S. Li, Y. Lin, Y.X. Tong, H. Liu, Enhanced efficiency of electron-hole separation in $\text{Bi}_2\text{O}_2\text{CO}_3$ for photocatalysis via acid treatment, *ChemCatChem* 10 (2018) 1982–1987.

[57] B. Lin, G.D. Yang, L.Z. Wang, Stacking-layer-number dependence of water adsorption in 3D ordered close-packed $\text{g-C}_3\text{N}_4$ nanosphere arrays for photocatalytic hydrogen evolution, *Angew. Chem. Int. Ed.* 58 (2019) 1–6.

[58] Y.L. He, Z.S. Fishman, K.R. Yang, B. Ortiz, C.L. Liu, J.L. Goldsamt, V.S. Batista, L.D. Pfefferle, Hydrophobic CuO nanosheets functionalized with organic adsorbates, *J. Am. Chem. Soc.* 140 (2018) 1824–1833.

[59] L.F. Wang, D.Q. He, W. Chen, H.Q. Yu, Probing the roles of Ca^{2+} and Mg^{2+} in humic acids-induced ultrafiltration membrane fouling using an integrated approach, *Water Res.* 81 (2015) 325–332.

[60] C. Zhu, Z. Jiang, L. Chen, K. Qian, J. Xie, L-Cysteine-assisted synthesis of hierarchical NiS_2 hollow spheres supported carbon nitride as photocatalysts with enhanced lifetime, *Nanotechnology* 28 (2017) 115708.

[61] W.X. Zou, Y. Shao, Y. Pu, Y.D. Luo, J.F. Sun, K.L. Ma, C.J. Tang, F. Gao, L. Dong, Crystal-plane-dependent metal oxide-support interaction in $\text{CeO}_2/\text{g-C}_3\text{N}_4$ for photocatalytic hydrogen evolution enhanced visible light photocatalytic hydrogen evolution via cubic CeO_2 hybridized $\text{g-C}_3\text{N}_4$ composite, *Appl. Catal. B* 218 (2017) 51–59.

[62] K. Zhao, J. Qi, H.J. Yin, Z.M. Wang, S.L. Zhao, X. Ma, J.W. Wan, L. Chang, Y. Gao, R.B. Yu, Z.Y. Tang, Efficient water oxidation under visible light by tuning surface defects on ceria nanorods, *J. Mater. Chem. A* 3 (2015) 20465–20470.

[63] F.F. Shi, L.L. Chen, M. Chen, D.L. Jiang, A $\text{g-C}_3\text{N}_4/\text{nanocarbon}/\text{ZnIn}_2\text{S}_4$ nanocomposite: an artificial Z-scheme visible-light photocatalytic system using nanocarbon as the electron mediator, *Chem. Commun.* 51 (2015) 17144–17147.

[64] X.J. She, J.J. Wu, H. Xu, J. Zhong, Y. Wang, Y.H. Song, K.Q. Nie, Y. Liu, Y.C. Yang, M.T.F. Rodrigues, R. Vajtai, J. Lou, D.L. Du, H.M. Li, P.M. Ajayan, High efficiency photocatalytic water splitting using 2D $\alpha\text{-Fe}_2\text{O}_3/\text{g-C}_3\text{N}_4$ Z-scheme catalysts, *Adv. Energy Mater.* 7 (2017) 1700025.